Bias adjustment of radar-based 3-hour precipitation accumulations

Iwan Holleman

Contents

Chapter 1

Introduction

Since June 2003 a daily gauge-adjusted accumulation product is operationally generated by the weather radar network of KNMI. The climatological network of manual rain gauges is used for the adjustment. The accumulations in the manual gauges are measured daily at 0800 UTC and reported by phone. The daily gauge-adjusted accumulation product is generated at 1400 UTC when the majority of the manual gauge observations have been reported. The radar-gauge adjustment algorithm is adapted from the scheme used operationally at the Baltex Radar Data Centre (Michelson *et al.*, 2000). An evaluation of the daily gauge-adjusted accumulation product is described in Holleman (2003). This daily accumulation product is rather useful for several (off-line) applications, e.g., evaluation of extreme cases and climatology, but it is not suited for real-time use.

Real-time spatial data on the precipitation depth is needed for many different applications, e.g.:

- Monitoring of severe weather by operational forecasters and issuing warnings ("Weeralarm").

- Automated warning system for water management authorities based on precipitation observations and forecasts ("Gevaarlijk Weer voor Waterbeheer").

- Quality evaluation of (automated) rain gauge observations.

- Input for Decision Support Systems used by water management authorities for real-time operation of pumps and discharge valves.

- Monitoring of wet deposition of chemicals and aerosols.

Since June 2003 a 3-hour accumulation product is also generated operationally at KNMI. This raw 3-hour accumulation product is updated hourly

and it is used by a number of internal and external customers. The raw radar accumulations occasionally suffer from severe underestimation of the precipitation depths which hampers the quantitative use of the product.

In this technical report it is demonstrated that the quality of the 3-hour accumulation product can be significantly enhanced by a straightforward gauge adjustment procedure. The KNMI network of automatic rain gauges is used for this real-time adjustment. The impact of the compositing algorithm on the quality has been assessed and a processing scheme for operational implementation is presented. The quality of the bias-adjusted 3-hour accumulation products is evaluated using both "dependent" and "independent" observations. A 6-year dataset of bias-adjusted accumulation products between 2000 and 2005 was used for the verification. It is concluded that the proposed scheme effectively removes the mean-field bias from the raw accumulation products and that it substantially reduces the standard deviation. Therefore it is highly recommended to add the bias-adjustment procedure to the operational 3-hour accumulation product. The outline of the remainder of the report is as follows:

- In Chapter 2 an overview of different sources of error affecting quantitative precipitation estimation by weather radar is given. The three most important errors are discussed in more detail.

- The operational generation and post-processing of radar-based accumulated precipitation products is described in Chapter 3.

- In Chapter 4 the operational rain gauge networks in The Netherlands that are maintained by KNMI are introduced and the statistical mean-field bias adjustment algorithm is discussed.

- The compositing of bias-adjusted precipitation accumulations from two or more radars is assessed in Chapter 5. A schematic overview of the processing chain for bias-adjusted accumulation composites is presented.

- A dataset containing 6 years (2000-2005) of weather radar accumulations and rain gauge observations has been used to evaluate the performance of the bias-adjustment algorithm. The results of this quantitative verification are presented in Chapter 6.

- In the last chapter the conclusions and recommendations for further application are made.

Chapter 2

Sources of error

In this chapter the sources of error affecting quantitative weather radar observations and quantitative precipitation estimation (QPE) in particular are discussed. First of all a comprehensive overview of the various sources of error is presented. Then the three most important errors for mid-latitude radars, most notably the vertical profile of reflectivity (VPR), the drop size distribution and thus the Z-R relationship, and attenuation by precipitation, are discussed in detail and illustrated by examples from the KNMI weather radars.

2.1 Overview of error sources

In the COST 717 report on "Weather Radar Data Quality in Europe: Quality Control and Characterization" by Michelson *et al.* (2005) a comprehensive overview of the various sources of error affecting the ability of radars to measure precipitation and influencing the accuracy of the measurements is given. Such errors are discussed by Browning (1987) and Joe (1996) among others. Since it is not easy to differentiate which error sources affect reflectivity measurements and which affect surface rainfall estimates, the two are combined in the listing below. Figure 2.1 illustrates some of the most important sources of error in weather radar observations. The overview of error sources given below is taken from Michelson *et al.* (2005). It touches upon the most important ones starting with the radar system itself and continuing out to various interactions with targets.

Electronics stability: Modern components vary slightly with time and with temperature. A monitoring system can keep the stability to within one dB or warn when tolerances are exceeded.
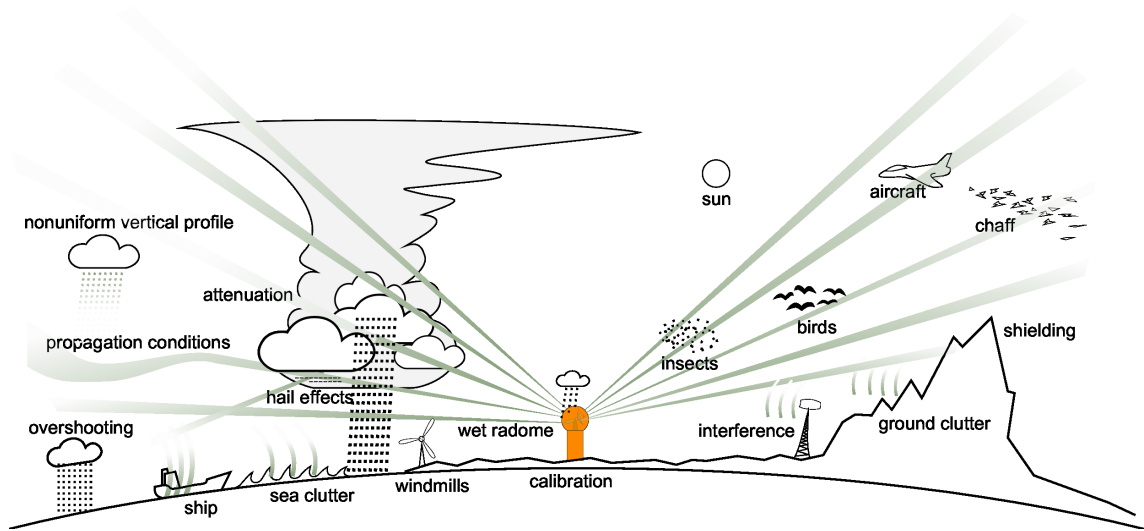
Figure 2.1: Schematic overview of the (main) sources of error affecting the quality of weather radar observations. This figure is taken from M. Peura (FMI).

Antenna accuracy: The antenna should be designed to minimize sidelobes. If its orientation accuracy is not regularly checked, data will be inaccurately navigated which will result in inaccurate location of measurements. The antenna alignment can be monitored operationally using sun signals (Holleman and Beekhuis, 2004; Huuskonen and Holleman, 2006).

Signal processing accuracy: The combination of the sampling capabilities of the radar hardware together with the performance of the signal processor will define the ability of the system to process data, to derive the most accurate radar observables, and to treat known errors. Regardless of the signal processor's performance, it must accurately interpret the Radar equation (see e.g. Doviak and Zrnić (1993)) in order to reduce the risk of error.

Electromagnetic interference: Other radars, microwave links, the sun, and military jamming can all cause interference which can result in errors.

Attenuation due to a wet or snow/ice covered radome: In heavy rain, a thin film of water will cover the radome, causing signal attenuation. In cold conditions, snow and ice may build up on top of the radome, also causing attenuation and limiting the quantitative use of reflectivity measurements.

8

Clutter: Ground clutter is usually strong due to the relative radar cross-section of the ground being much greater than that from meteorological targets, and despite echoes from the ground being generated from sidelobe radiation which is much weaker than that from the main lobe. Ground clutter can be minimized through intelligent radar siting, Doppler suppression, and through the use of post-processing methods such as static clutter maps.

Anomalous propagation: Specific atmospheric temperature and/or moisture gradients will cause part of the radar beam to propagate along a non-normal path. If the fraction of the beam that is refracted downward (super-refraction) is refracted sufficiently, the radiation will illuminate the surface and return signals to the radar from distances further than are normally associated with ground clutter targets. The (anomalous propagation) clutter removal scheme used operationally by KNMI is described extensively in Holleman and Beekhuis (2005).

Shielding: If the radar siting is of poor quality, nearby objects like trees, topography, and buildings and other structures can block the radar beam in whole or in part, causing shielding of sectors of interest. Regardless of siting quality, anomalous propagation can still cause problems at distant ranges.

Other non-precipitation echoes: Such echoes can originate from birds, insects, chaff (strips of metal foil used by the military), and refractive inhomogeneities known as clear air echoes. These echoes are often not static in space, which means that they cannot be effectively treated using Doppler techniques. They are, however, often easily identifiable by an operator.

Attenuation by precipitation: Heavy rain, graupel and hail can attenuate energy, leading to strong underestimation of precipitation intensities. Especially in hail, where scattering takes place in the Mie region, the scattered energy can be attenuated to the point of virtual extinction over the return path. Shorter wavelengths (X and C bands) are more seriously affected.

Z-R relation: This relation, expressed in the form $Z = aR^b$, provides the foundation for relating radar reflectivity Z to rainfall intensity R. Z and R are usually assumed to be functions of the 6th and roughly 4th moment of the drop size distribution (DSD), respectively. Thus, the DSD will fundamentally influence Z, and the Z-R relation itself can be very sensitive to the choice of coefficients a and b.

Precipitation phase: Operational, single polarization systems are usually unable to classify hydrometeor type. Rain, snow, melting snow, graupel and hail may thus all be present, yet the radar can only consider them as being one type. This leads to uncertainties in the selected Z-R relation when converting reflectivity to precipitation intensity.

The melting layer: This factor is specific to the region where snow melts to rain. The extremities of a snowflake melt first, causing a film of water to coat the particle before it implodes into a raindrop. Since water is a much more conductive medium than ice, this causes strong reflectivities in radar data and an effect known as the "bright band" where this region is found at more-or-less uniform heights/ranges. In southern Europe, the melting layer exists throughout the year, and can reach up to above four km during summer. It is often absent or very close to the surface during the winter in northern Europe, and seldom reaches above three km during summer.

Beam filling and overshooting: These two effects are problems which increase in severity with increasing range from the radar, as the beamwidth increases. Beam filling occurs where the scale of precipitation is small relative to the pulse volume, for example in convection. Overshooting, in whole or in part, occurs where the precipitation is shallow in relation to the pulse volume. Overshooting is thus a greater problem in cold climates, as winter snow is usually considerably shallower than summer rain.

Non-uniformly vertically distributed precipitation: Several of the above-mentioned factors can combine and lead to problems interpreting the observable as being valid as a surface measurement. This leads to problems applying the radar equation which must usually be neglected. These errors also lead to representativeness problems if the objective is to achieve a measurement which is applicable as a surface estimate, and such problems are related to the vertical profile of reflectivity (VPR) and its characteristics.

The three most important errors for mid-latitude radars, most notably the vertical profile of reflectivity (VPR), the drop size distribution and thus the Z-R relationship, and attenuation by precipitation, are discussed in detail and illustrated by examples from the KNMI weather radars in the following sections.
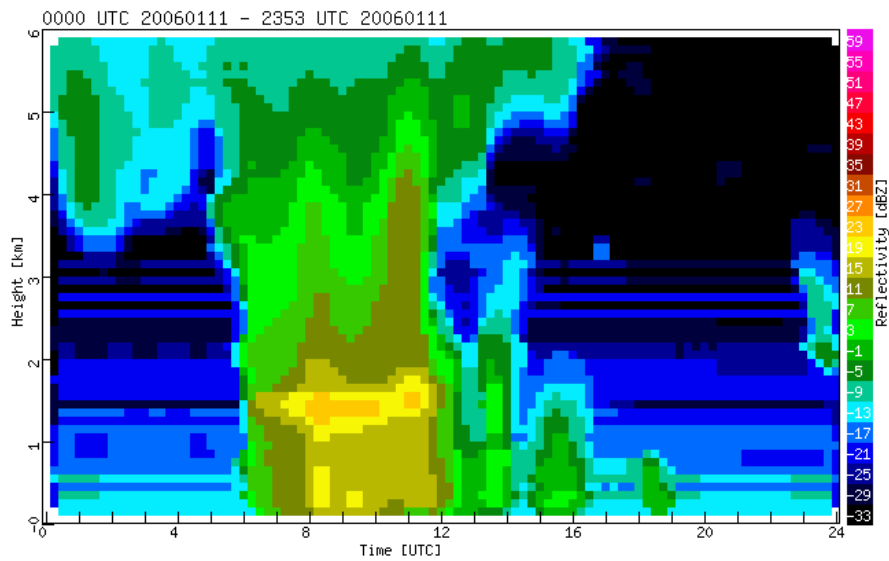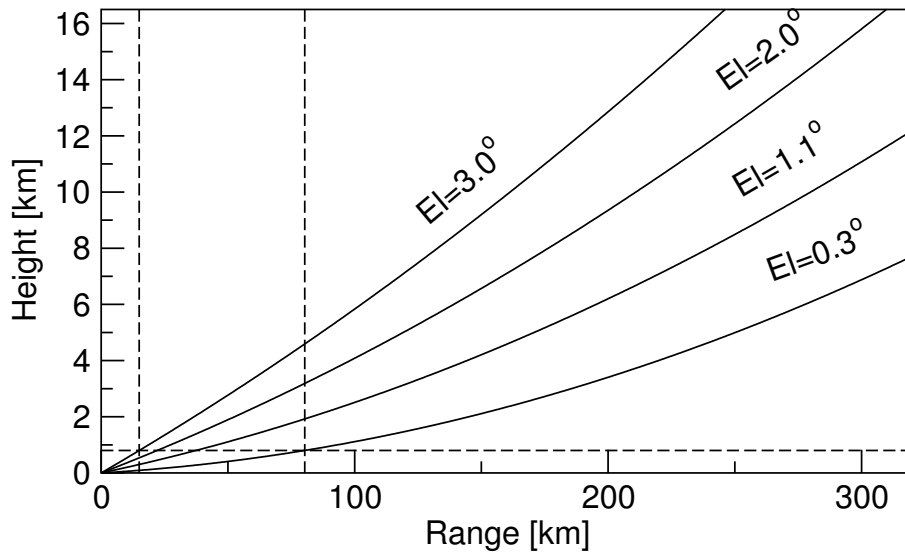
Figure 2.2: The upper frame shows the calculated beam height as a function of range for the four elevations used to construct the pseudoCAPPI images. The lower frame shows a time-height plot of the mean reflectivity above the weather radar in De Bilt for 11 January 2006.

11

2.2   Vertical Profile of Reflectivity (VPR)

The Vertical Profile of Reflectivity (VPR) is, especially at higher latitudes, the major source of error in quantitative precipitation estimates deduced from weather radar observations (Joss and Waldvogel, 1990; Koistinen, 1991). The KNMI weather radars in De Bilt and Den Helder perform a 4-elevation reflectivity scan every 5 minutes. From these scans pseudoCAPPI (pseudo Constant Altitude Plan Position Indicator) images are produced with a spatial resolution of 2.5 km and a target height of 0.8 km above antenna level. In upper frame of Figure 2.2 the calculated beam height as a function of range is shown for the four elevations used to construct the pseudoCAPPI images. These four elevations are 0.3, 1.1, 2.0 and 3.0 degrees. It can be seen that the target height of the pseudoCAPPI (marked by the horizontal dashed line) can be reached up to a range of 80 km only. At longer ranges the height of observation will increase and in the presence of a significant gradient in the vertical profile of reflectivity, this will typically give rise to an underestimation of the accumulated precipitation at long ranges.

The lower frame of Figure 2.2 shows a time-height plot of the mean reflectivity above the weather radar in De Bilt for 11 January 2006. The mean reflectivity as a function of height is calculated from raw volume data by linear averaging the available reflectivity observations in disks with a thickness of 200 m and a radius of 25 km. On this day a warm front and a cold front due to a deep depression at the coast of Norway passed over The Netherlands within a few hours. From the figure it is evident that it was raining continuously in De Bilt between 06 and 14 UTC and that three weak showers occurred between 14 and 20 UTC. Non-uniform reflectivity profiles are observed during the whole day: between 00 and 06 UTC reflectivity is only observed aloft, between 06 and 12 UTC an intense band of reflectivity is observed around an altitude of 1.5 km, and the afternoon showers have a very limited vertical extent (< 1.5 km). The intense band of reflectivity is caused by melting precipitation and it is commonly known as the bright band (see previous section). The non-uniform reflectivity profiles are caused by interaction between droplets, updrafts and downdrafts, evaporation and accretion of drops under the cloud base, and melting precipitation. As a result, the observed reflectivity will (strongly) depend on the height and thus on the range.

Many different techniques have been developed to estimate the vertical profile of reflectivity and to subsequently correct the radar precipitation estimates for this profile. The vertical profile of reflectivity can be estimated using climatological profiles, mean reflectivity profiles or local profiles obtained at short ranges (Vignal *et al.*, 2000; Vignal and Krajewski, 2001; Koistinen

et al., 2003). Alternatively, the VPR can be determined using a sophisticated technique based on inverse theory (Andrieu and Creutin, 1995; Vignal *et al.*, 1999). Kitchen *et al.* (1994) have developed a method to assign an idealized VPR profile to each radar pixel based on satellite derived cloud top height, model freezing level height, and orographic contribution dependent on model winds. On the other hand, gauge adjustment techniques have been developed which correct the radar precipitation estimates using a second-order polynomial in range, e.g. Michelson *et al.* (2000). Because the height of the radar beam increases approximately quadratic with range, these gauge adjustment techniques basically correct for a linear gradient in the vertical profile of reflectivity.

In a flat country, like The Netherlands, application of a sophisticated VPR adjustment technique may be overdone because at 150 km range only a translation from 2 km altitude down to ground level is needed, which is actually within the radar beam width at that range. A straightforward technique for VPR adjustment based on the analysis of accumulated pseudoCAPPI data at two different heights has been proposed by Holleman (2004). The extracted VPR gradient is used to perform a range and azimuth dependent adjustment using a purely analytical expression. The application of the dual-CAPPI technique has been illustrated using a case of stratiform precipitation and a strong bright band interference. A preliminary verification has indicated that the dual-CAPPI technique performs rather good for cases with stratiform precipitation.

2.3 Z-R Relation

The translation of radar reflectivity Z observations into rainfall intensity R is non-trivial and depends heavily on the actual drop size distribution (DSD). The most famous publication on this subject "The Distribution of Raindrops with Size" by Marshall and Palmer (1948) is almost 60 years old. The radar reflectivity Z and the rainfall rate R can be written as moments of the drop size distribution $N(D)$ (Doviak and Zrnić, 1993; Uijlenhoet, 1999):

$$Z = \int_0^\infty N(D) \cdot D^6 \, dD \tag{2.1}$$

$$R = 36 \times 10^{-4} \int_0^\infty N(D) \cdot \frac{\pi}{6} D^3 \cdot v(D) \, dD \tag{2.2}$$

$$\simeq 6 \times 10^{-4} \pi \alpha \int_0^\infty N(D) \cdot D^{3+\beta} \, dD \tag{2.3}$$

13
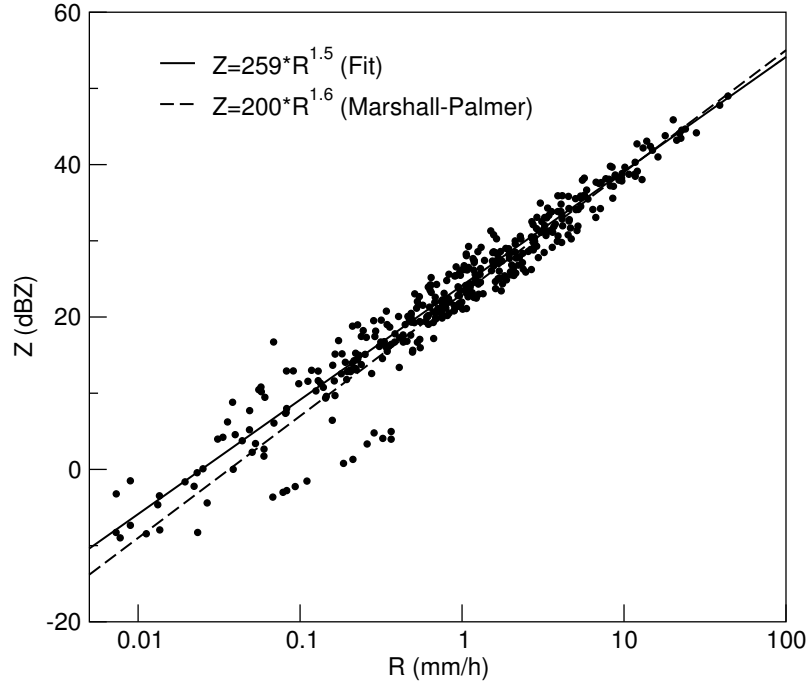
Figure 2.3: Calculated radar reflectivity Z in dBZ versus rainfall intensity R obtained from raindrop measurements at De Bilt (Wessels, 1972)

where D represents the drop size diameter and the terminal fall speed of drops $v(D)$ has been approximated by a power law:

$$v(D) \simeq \alpha D^{\beta} \tag{2.4}$$

where the speed is given in m/s and the diameter in mm. According to Atlas and Ulbrich (1977) the constants α and β should be taken as 3.778 and 0.67, respectively. The above equations can be evaluated once the drop size distribution is known. Marshall and Palmer (1948) proposed a simple exponential form of the drop size distribution which is widely accepted:

$$N(D) = N_0 \exp(-\Lambda D) \tag{2.5}$$

where the drop density N_0 is equal to 8×10^3 mm^{-1} m^{-3} and $\Lambda = 4.1 R^{-0.21}$ mm^{-1} depends on the rainrate R in mm/h. Numerous other functional forms for the DSD have been proposed over the last decades which are more complicated, e.g. gamma functions. Because Equation 2.5 allows an analytical evaluation of the moments $M(x)$ of the drop size distribution it is commonly used:

$$M(x) = \int_0^{\infty} N_0 \exp(-\Lambda D) \cdot D^x \, dD = \frac{N_0 \Gamma(x+1)}{\Lambda^{x+1}} \tag{2.6}$$

14

where $\Gamma(x)$ represents the Gamma function, see Press *et al.* (1992). For the radar reflectivity Z and the rainfall rate R, the following expression can thus be derived:

$$Z \; = \; M(6) = \frac{N_0 \Gamma(7)}{\Lambda^7} = \frac{720 N_0}{\Lambda^7} \tag{2.7}$$

$$R \; = \; M(3 + \beta) = \frac{6 \times 10^{-4} \pi \alpha N_0 \Gamma(4 + \beta)}{\Lambda^{4+\beta}} \tag{2.8}$$

Using these two equations a relation between Z and R can be derived in two distinctly different ways. When $\Lambda = 4.1 \times 10^3 R^{-0.21}$ is substituted in the upper equation, it is straightforward to obtain the following Z-R relation (Marshall and Palmer, 1948):

$$Z = 296 R^{1.47} \tag{2.9}$$

where the reflectivity Z is given in mm^6/m^3 and the rainrate R in mm/h. Alternatively, when equations 2.7 and 2.8 are used to eliminate Λ, the following Z-R relation is obtained:

$$Z \; = \; 720 N_0 \left[6 \times 10^{-4} \pi \alpha N_0 \Gamma(4 + \beta) \right]^{-7/(4+\beta)} R^{7/(4+\beta)} \tag{2.10}$$

$$= \; 237 R^{1.50} \tag{2.11}$$

where $\Gamma(4.67) = 14.782$ has been used. Evidently the two Z-R relations are not automatically identical. Uijlenhoet and Stricker (1999) have investigated this inconsistency of the Z-R relations in great detail and have developed a consistent rainfall parameterization.

The "power law" form of the Z-R relation as obtained above is widely accepted as a semi-empirical relation:

$$Z \; \equiv \; a R^b \tag{2.12}$$

$$\tilde{Z}[\text{dBZ}] \; \equiv \; 10 \, {}^{10}\!\log Z = 10 \, {}^{10}\!\log a + 10 \, b \, {}^{10}\!\log R \tag{2.13}$$

but for the prefactor a and exponent b many different values, ranging between 100-500 and 1.2-1.7 for a and b, respectively, have been reported in literature (Collier, 1989). The relation $Z = 200 R^{1.6}$ is widely accepted. The variability of the Z-R relation originates from (local/temporal) differences in the drop size distribution due the precipitation type and climatological circumstances. In Figure 2.3 the Z-R relation as obtained from drop size distribution measurements at De Bilt is visualized. Between 1968 and 1969 Wessels (1972) has measured approximately 0.5 million droplets and estimated their sizes from the imprints on filter paper. From these measured drop size distributions the

radar reflectivity Z and rainfall rate R can be calculated using equations 2.2 and 2.3, respectively. Figure 2.3 show the relation between Z in units of dBZ and R in mm/h. A good correlation between Z and R is observed and it is clear that a power law fits the data rather well. Finally, it should be noted that the scatter of the data around the fit implies that for individual rainfall events the deviations from the fitted Z-R relation can be large (up to 50%).

2.4 Attenuation

The radio frequency radiation transmitted and received by a weather radar is scattered by precipitation. During very strong precipitation, this scattering can become so strong that the radar beam gets attenuated. Attenuation of the radar beam causes underestimation of the precipitation intensity or even disappearance of the rain cells behind very strong cells.

In Figure 2.4 a series of reflectivity composite images during an event of severe attenuation is displayed. These composites are generated by taking the maximum observed values from the radars in De Bilt and Den Helder. On 17 July 2004 a severe squall line passed from southwest to northeast over The Netherlands producing very strong wind gusts ($\simeq$30 m/s), intense precipitation ($\simeq$50 mm/h), severe thunder and lightning, and large hail. The upper-left image from 1645 UTC clearly shows the severe squall line with a length of several hundred kilometers and a width of approximately 20 km. Note that the squall line is perfectly aligned with the intersecting line between both radars (marked by crosses). 15 Minutes later, see upper-right image from 1700 UTC, the squall line has disappeared almost completely from the reflectivity composite due to severe attenuation. At the same time, the precipitation area in the northeast is unaffected because it is observed in a direction (almost) perpendicular to the squall line. In the last image, lower-left from 1730 UTC, the squall line has reappeared because it has passed the intersection line between both radars.

The attenuation of received radar echoes due to the propagation through the atmosphere is described by (Hitschfeld and Bordan, 1954; Berne and Uijlenhoet, 2006):

$$Z_a(r) = Z(r) \exp\left(-\frac{2 \log 10}{10} \int_0^r \kappa dr\right) \qquad (2.14)$$

where $Z_a(r)$ represents the attenuated reflectivity at range r from the radar in mm^6/m^3 and κ is the one-way, atmospheric attenuation coefficient in dBZ/km. The atmospheric attenuation is due to atmospheric gasses, most

16
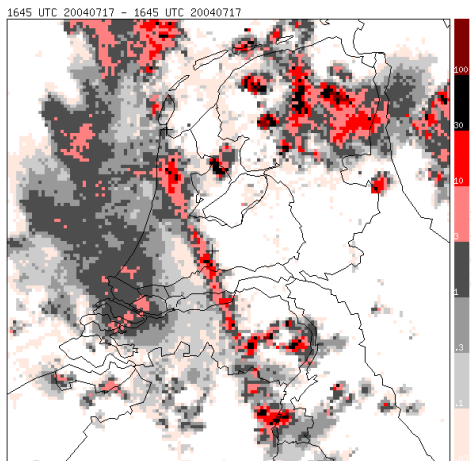
1645 UTC   1700 UTC
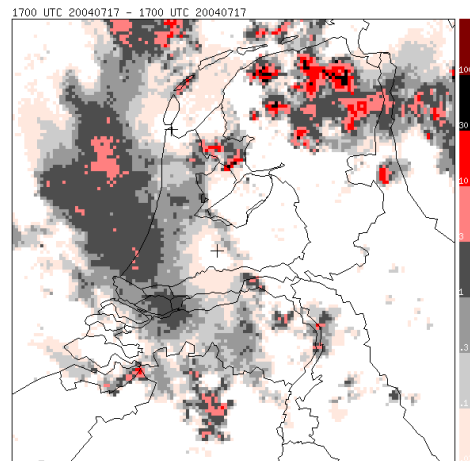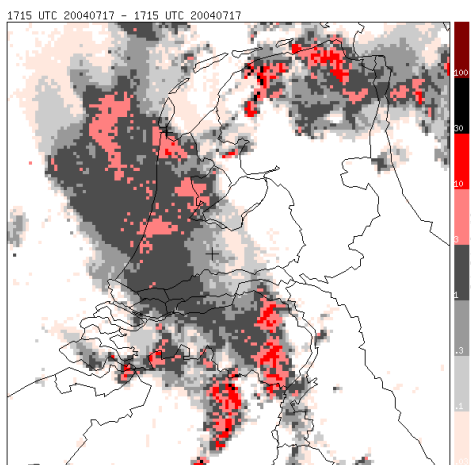
1715 UTC   1730 UTC
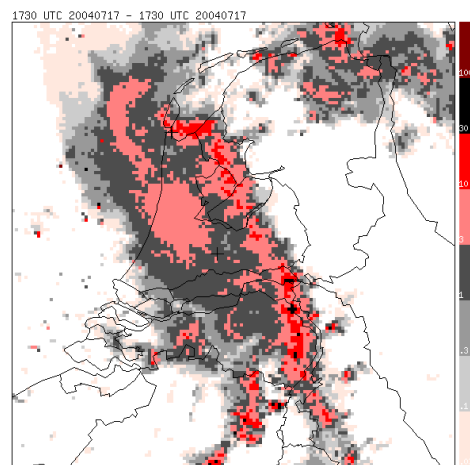
Figure 2.4: A series of reflectivity composite images (from De Bilt and Den Helder radars) during an event of severe attenuation on 17 July 2004 is displayed.

17

notably water vapor and oxygen, to clouds, and to rain (Hitschfeld and Bordan, 1954). The attenuation due to rainfall is the most variable and can occasionally be strong at C-band. A "power law" form can be used to approximate the one-way attenuation due to rainfall:

$$\kappa \equiv \gamma Z^{\delta} = 2.0 \times 10^{-5} Z^{0.75} \tag{2.15}$$

where typical values for γ and δ at C-band have been extracted from Doviak and Zrnić (1993). Combining these two equations and taking the natural logarithm gives:

$$\log[Z_a(r)] = \log[Z(r)] - \frac{2\gamma \log 10}{10} \int_0^r Z(r)^{\delta} dr \tag{2.16}$$

where $y(r)$ is introduced. Hitschfeld and Bordan (1954) have shown that this equation can be inverted by differentiation and substitution of $y = \log(Z_a)$ and $x = Z^{-\delta}$:

$$x(r) = \left[1 - \frac{2\gamma\delta \log 10}{10} \int_0^r \exp[\delta y(r)] dr\right] / \exp[\delta y(r)] \tag{2.17}$$

and thus the following expression for $Z(r)$ as a function of $Z_a(r)$ is obtained:

$$Z(r) = Z_a(r) / \left[1 - \frac{2\gamma\delta \log 10}{10} \int_0^r Z_a(r)^{\delta} dr\right]^{1/\delta} \tag{2.18}$$

This equation could be used to correct reflectivity for attenuation but the denominator can be close to zero. This makes a correction algorithm for attenuation potentially highly unstable (Hitschfeld and Bordan, 1954) which has also been observed for C-band and X-band radars (Delrieu *et al.*, 1999; Berne and Uijlenhoet, 2006). For the (near) future, dual-polarization weather radars offer promising new possibilities to correct for attenuation due to rainfall (Gorgucci *et al.*, 1998; Bringhi and Chandrasekar, 2001).

The radar antenna is normally positioned in a radome in order to protect it from rain and wind. The absorption by the dry radome is typically a few tenths of a dB for a C-band radar, while for a wet radome values of up to 5 dB for two-way transmission have been found (Manz *et al.*, 1998; Germann, 1999). Therefore the attenuation due to a (wet) radome can easily be stronger than the attenuation in the atmosphere.

Chapter 3

Accumulation and post processing of radar data

In this chapter the operational generation of radar reflectivity images and accumulated precipitation products are described briefly. In addition, some post processing of the accumulated precipitation products to reduce the impact of spurious signals close to the radar is presented.

3.1   Accumulation of radar data

KNMI operates two identical C-band Doppler weather radars from SELEX, formerly known as Gematronik GmbH. The De Bilt radar is located at a latitude of 52.10N and a longitude of 5.18E. The Den Helder radar is located at a latitude of 52.96N and a longitude of 4.79E. The received signal is digested by a RVP6 radar processor (Sigmet, 1998) and the generation of products is done using Rainbow software (Gematronik, 2003). Currently KNMI is preparing a technical upgrade of the weather radar systems which are now running for almost 10 years. The purpose of the upgrade is to ensure that the weather radars can operate for another 10 years. The upgrade will consist of a renewal of the radar (scan) controller, the signal processor, and the product generator.

The operational reflectivity scan for precipitation estimation consist of a four elevation scan (0.3, 1.1, 2.0, and 3.0 degrees) which is performed every 5 minutes. From these scans pseudoCAPPI images are produced with a target height of 800 m above antenna level. Details on the geographical projection of the radar images are given in Appendix A. Ground clutter and anomalous propagation clutter are removed from the pseudoCAPPI images using a stepwise procedure described in Wessels and Beekhuis (1994); Holleman and

5-Minute reflectivity   3-Hour accumulation
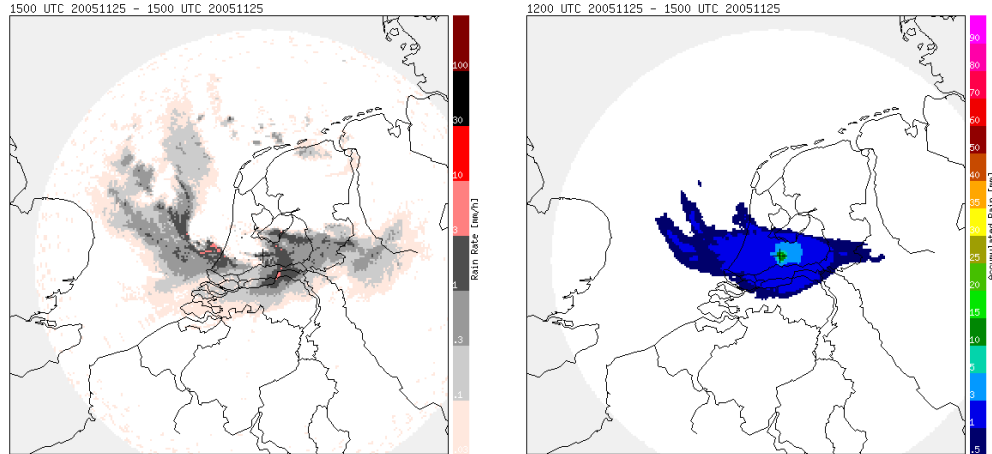
Figure 3.1: The left image shows a 5-minute reflectivity product from the radar in De Bilt at 1500 UTC on 25 November 2005. The right image shows the accumulated precipitation between 1200 and 1500 UTC on the same day.

Beekhuis (2005). An example of a pseudoCAPPI product from the radar in De Bilt is displayed in Figure 3.1. During the technical upgrade the operational clutter removal scheme will be replaced by a method for 3-dimensional polar data as described in Holleman and Beekhuis (2005). This new scheme produces cleaner reflectivity images where the residual clutter close to the radar and especially the sea clutter are removed more effectively.

Before accumulation the radar reflectivity values are converted to rainfall intensities using a fixed "Marshall-Palmer type" Z-R relationship:

$$Z = 200R^{1.6} \tag{3.1}$$

with the radar reflectivity Z in mm^6/m^3 and rainfall rate R in mm/h. To avoid the accumulation of noise, radar reflectivities below 7 dBZ (0.1 mm/h) are not accumulated. Similarly, the impact of large hail or residual strong clutter on the precipitation estimates is suppressed by maximizing the reflectivity to 55 dBZ (100 mm/h). Based on these data, 3-hour accumulations are calculated every hour and a 24-hour accumulation is produced at 0800 UTC only. A 5-point median filter is applied to the accumulated precipitation products to reject local outliers due to e.g. accumulated (ground) clutter. When one or more 5-minute pseudoCAPPI products are missing for a certain accumulation period (minimum availability: 80%), the resulting accumulated precipitation product is scaled by the fraction of missing
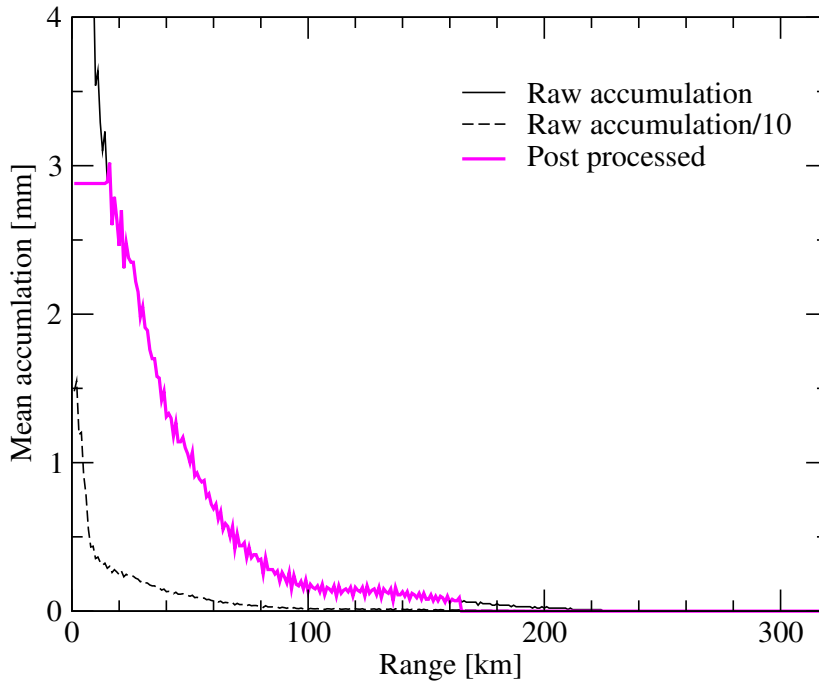
Figure 3.2: Mean accumulated precipitation as a function of range from the radar in De Bilt between 1200 and 1500 UTC on 25 November 2005 (see Figure 3.1). The observed precipitation has been averaged in azimuthal direction.

pseudoCAPPI products. An example of a "raw" accumulated precipitation product from the radar in De Bilt is displayed in Figure 3.1.

3.2   Post processing of raw accumulations

From the example accumulation shown in the right image of Figure 3.1 it is evident that the largest precipitation depths are observed close to the radar in De Bilt (location marked by the cross). Figure 3.2 shows the mean accumulated precipitation as a function of range from the radar in De Bilt for the same case. Data are shown for the full operational range of the KNMI weather radars, i.e., 320 km. The observed accumulated precipitation has been averaged in azimuthal direction. From the solid and dashed black curves in the figure, it is evident that the raw accumulation exhibits a sharp maximum (> 15 mm) at short range from the radar (< 15 km). This artifact is caused by accumulation of spurious echoes at short ranges from the radar. These spurious echoes mainly originate from transmitter noise, sidelobe clut-

21

ter, and measurement below the target altitude of the pseudoCAPPI (see Figure 2.2).

The mean-field bias correction method, which will be described in the next chapter, cannot correct for these spurious echoes at short ranges and therefore a dedicated post processing procedure has been developed to reduce the impact of these spurious echoes. Within a predefined range from the radar, default 15 km, the azimuthal-mean accumulation is calculated at 1 km intervals. When the azimuthal-mean accumulation is higher than that at the predefined range, the corresponding pixel values are rescaled such that the mean accumulation becomes equal to that at the predefined range. The effect of this post processing on the mean accumulation as a function of range is depicted by the blue curve in Figure 3.2.

In Section 2.2 it has been detailed that the radar observation become unreliable at longer ranges due to increasing height of the observations and non-uniform Vertical Profiles of Reflectivity. It is therefore necessary to limit the range of the weather radars for quantitative precipitation estimation (QPE). The default maximum range for QPE has been set to 165 km. With this value for the maximum range, the whole of The Netherlands is just covered by the composite data from the two operational weather radars of KNMI. The effect of this range limitation can also be seen from the blue curve in Figure 3.2. Figure 3.3 shows the raw (left image) and post processed (right image) accumulation products for 1500 UTC on 25 November 2005, i.e., the case used in Figures 3.1 and 3.2. The limitation of the range can be seen from appearance of the light gray "no data" area and the spurious echoes close to the radar are clearly suppressed. The parameters and their default values for the accumulation of radar data and the post processing are listed in Table 3.1.

Raw   Post processed
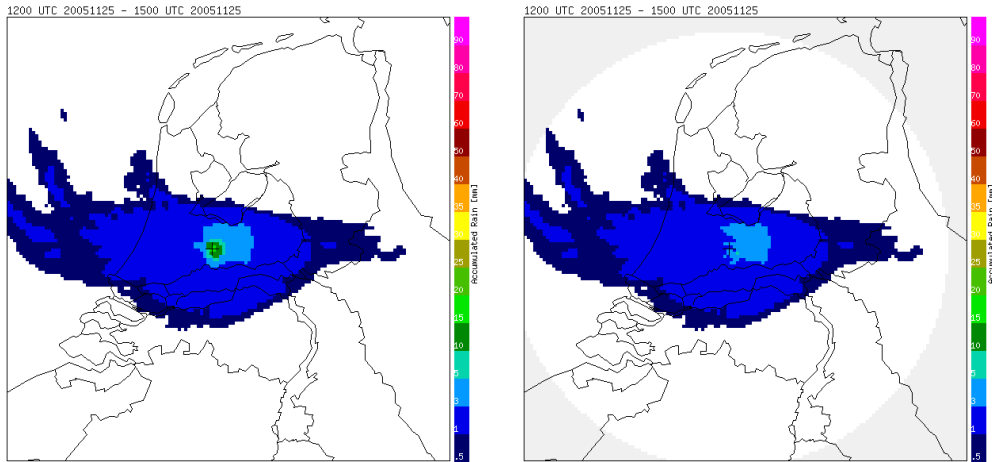
Figure 3.3: Raw (left) and post processed (right) accumulated precipitation products from the radar in De Bilt between 1200 and 1500 UTC on 25 November 2005 (matching Figures 3.1 and 3.2). The images have been zoomed to better show the relevant area around The Netherlands.

Table 3.1: Default values of the parameters for the accumulation and post processing of precipitation data.

Parameter	Description	Value
Z_t	Reflectivity threshold for accumulation	7 dBZ
Z_x	Maximum reflectivity in accumulation	55 dBZ
a	Prefactor in Z-R relation	200
b	Exponent in Z-R relation	1.6
F_a	Minimum fraction of available CAPPIs	0.80
N_f	Number of pixels for median filter	5
R_s	Maximum range for rescaling	15 km
R_x	Maximum quantitative range	165 km

23

Chapter 4

Mean-field bias adjustment

The mean-field bias of the post-processed accumulated precipitation products will be corrected using observations from automatic precipitation gauges. Using this statistical approach, the gross error in the radar quantitative precipitation estimates is corrected. First of all, the rain gauge networks in The Netherlands that are maintained and operated by KNMI will be introduced. Then the mean-field bias adjustment algorithm will be discussed.

4.1   Available rain gauge data

KNMI operates two independent networks for the observation of precipitation depth at different temporal and spatial resolutions. The climatological network is a dense network of about 325 volunteers who report the accumulated precipitation daily at 0800 UTC using manual precipitation gauges. The density of these climatological stations is about one station every 100 km^2. The automatic weather station (AWS) network of KNMI is a network of 35 stations which report every 10 minutes a number of meteorological quantities, amongst others (dewpoint) temperature, wind speed and direction, cloud base and cover, and precipitation depth. Figure 4.1 shows two maps of The Netherlands with the locations of the manual and automatic rain gauges.

The conventional manual rain gauges as used for the climatological network consists of a funnel with a horizontal entry area of 0.02 m^2 and a collection reservoir. The amount of precipitation is determined manually using a measuring cylinder with a resolution of 0.1 mm. Due to representativeness errors or losses on pouring the precipitation into the cylinder, the actual observation accuracy is more than 0.1 mm. The automatic rain gauges determine the amount of precipitation by measuring the position of a floater placed in a measuring cell. The floater is linked to a potentiometer. Solid

Synoptical   Climatological
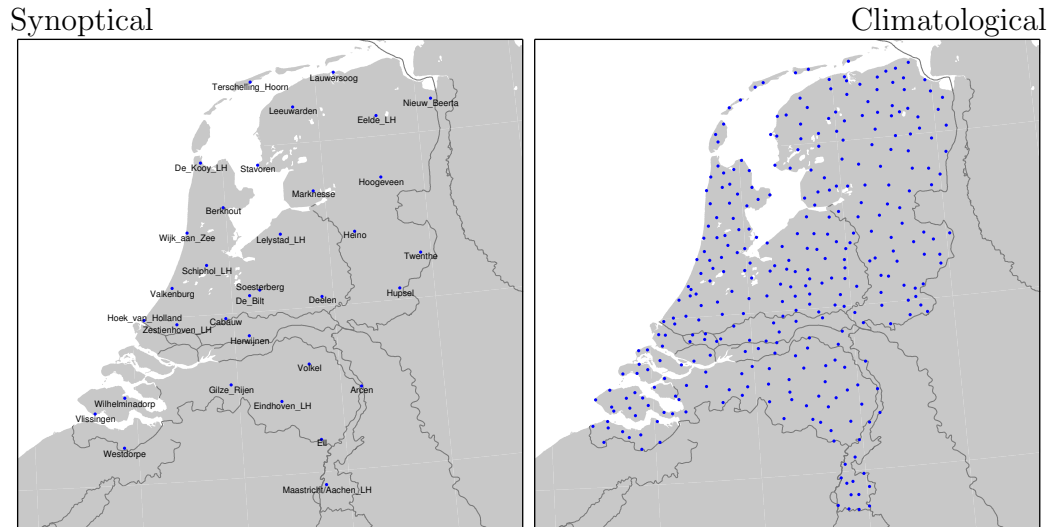
Figure 4.1: The left map shows the Dutch national synoptical network with electronic precipitation gauges (35) and the right map shows the Dutch climatological network of manual precipitation gauges (325).

precipitation is melted by heating of the funnel. An accuracy of 0.2 mm is specified for the automatic rain gauges. More details on the KNMI rain gauge sensors and networks can be found in the "Handbook of the Meteorological Observation" (Benschop, 2000).

4.2 Bias adjustment algorithm

A mean-field bias adjustment algorithm is used to correct the gross error in the post processed 3-hour precipitation accumulations as observed against the automatic rain gauge observations. This statistical approach is straightforward and effective. When physical correction methods, e.g. for VPR or attenuation, suited for operational implementation become available in the future they will reduce the need for this bias adjustment. Mean field bias adjustment of radar-based quantitative precipitation estimates is widely used, see for instance Fulton *et al.* (1998); Harrison *et al.* (2000); Chumchean *et al.* (2006).

The bias-adjusted precipitation estimates are calculated from the uncorrected (post processed) precipitation estimates as follows:

$$\tilde{R}(i,j) \equiv \frac{R(i,j)}{F} \tag{4.1}$$

26

where $\tilde{R}(i,j)$ and $R(i,j)$ represent the bias-adjusted accumulation and uncorrected accumulation, respectively, of the pixel at image coordinates (i,j). The bias-adjustment factor F is constant for the whole image, i.e., "mean field" correction, and has to be determined from a comparison between collocated radar and gauge observations. Assume that for a certain accumulation period, an uncorrected radar accumulation product $R(i,j)$ and observations from a number of rain gauges G_n are available. The mean-field bias B of the adjusted radar accumulation can then be calculated as follows:

$$B \equiv \frac{1}{N} \sum_{n=1}^{N} (\tilde{R}(i_n, j_n) - G_n) \qquad (4.2)$$

where (i_n, j_n) are the image coordinates of rain gauge n and N is the number of available rain gauges. An equation for the bias-adjustment factor F can be derived from the requirement that the mean-field bias should be zero after adjustment $(B = 0)$:

$$0 \equiv \frac{1}{N} \sum_{n=1}^{N} (\frac{1}{F} \cdot R(i_n, j_n) - G_n) \qquad (4.3)$$

and by rearrangement one finds the following equation for the bias-adjustment factor:

$$F = \frac{\sum_{n=1}^{N} R(i_n, j_n)}{\sum_{n=1}^{N} G_n} \qquad (4.4)$$

where basically the total amount of precipitation in the radar image and in the rain gauge network are matched. The bias-adjustment factor can only be calculated when the denominator is not zero and it only makes sense when both the numerator and denominator are not close to zero. By default, F is only calculated when both its numerator and denominator are larger than 5.0 mm, which corresponds to roughly 0.15 mm per gauge for a network of 35 rain gauges, and otherwise F is set to 1. When presenting a distribution of obtained bias-adjustment factors it is often beneficial to make them more symmetrical (around unity) by using a decibel-scale:

$$\tilde{F}[\text{dB}] \equiv 10 \; ^{10}\log F \qquad (4.5)$$

and thus a neutral adjustment factor (unity) corresponds to 0 dB.

Chapter 5

Compositing of radar accumulations

In this chapter the compositing of bias-adjusted precipitation accumulations from two or more radars is discussed. The pros and cons of different ways to combine data from different radars in overlapping regions are highlighted, and a choice for the optimum compositing algorithm is made. Finally, a schematic overview of the processing chain for bias-adjusted accumulation composites is presented.

5.1   Compositing algorithms

After application of the mean-field bias correction, adjusted precipitation accumulation products are available from each weather radar, i.e., De Bilt and Den Helder. An example of these bias-adjusted precipitation accumulation products from both radars is presented in Figure 5.1. It is evident from the figure that both weather radars have an overlapping coverage for a major part of The Netherlands. In this area the precipitation observations of both weather radars can be compared and striking differences can be seen. Above the Northsea (Western part of the images), the radar in Den Helder observes precipitation depths between 20 and 25 mm while De Bilt observes a mere 5 to 10 mm. On the other hand, the radar in De Bilt observes a precipitation maximum (25 mm) in the central part of The Netherlands which is hardly seen by the other radar. These differences can be attributed to a non-uniform Vertical Profiles of Reflectivity (VPR) and an increasing height of the observations at longer ranges (see Section 2.2). On this winter day with extreme snowfall and strong VPR gradients, the quantitative range of the weather radars was exceptionally short.

De Bilt   Den Helder
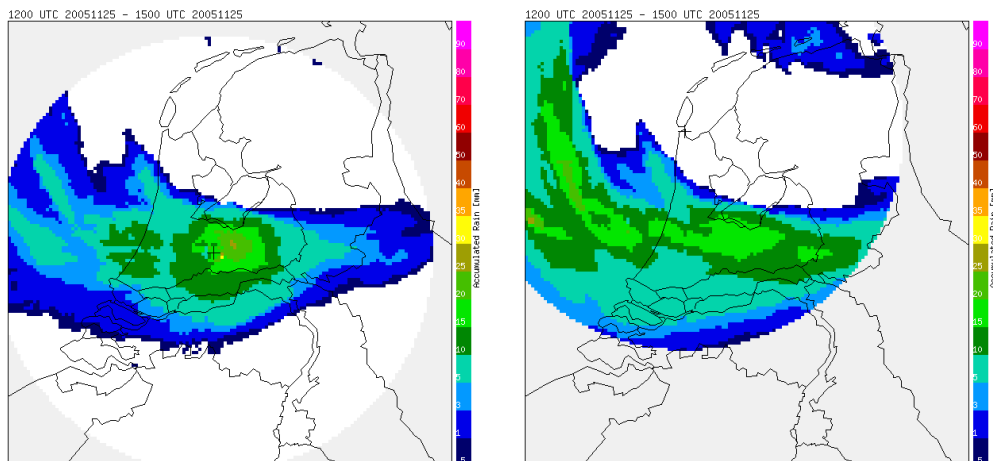
Figure 5.1: Example of bias-adjusted precipitation accumulation products
from the radars in De Bilt (left) and Den Helder (right) for 1500 UTC on 25
November 2005.

The operational bias-adjusted accumulation product will be composed of
the accumulation products from the individual weather radars. It is evident
from the images in Figure 5.1 that the products from the different radars al-
ready have a common geographical projection (details given in Appendix A).
Then the question remains how to combine the pixel values from different
radars in the overlapping regions. Several ways to combine the pixel values
in a radar composite can be thought of:

Maximum Use the maximum of the available pixel values in the composite
product. This method is commonly used to build composites of radar
reflectivity products and it has the inherent advantage that attenua-
tion of one radar is compensated by another radar. For bias-corrected
precipitation accumulations, this method has the disadvantage that it
introduces a bias because the "maximum" of two distributions without
a bias will have a positive bias.

Mean Use the mean of the available pixel values in the composite product.
This method is occasionally used to build composites of radar products.
For bias-corrected accumulation products, this method has the advan-
tage that it does not introduce a bias in the composite. Attenuation of
one radar is, however, only partly compensated by other radars.
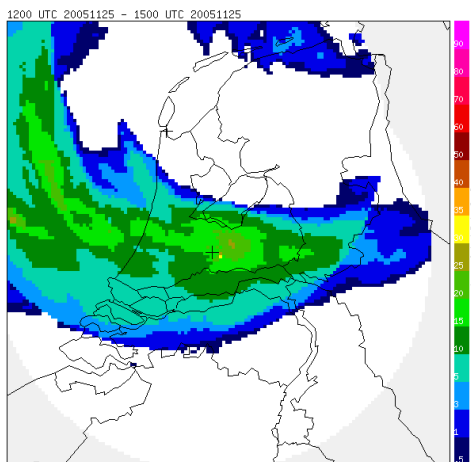
Maximum   Mean
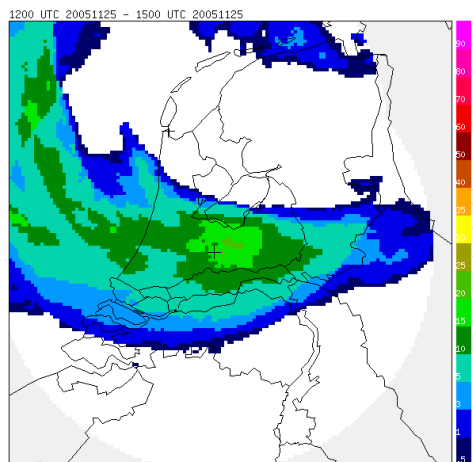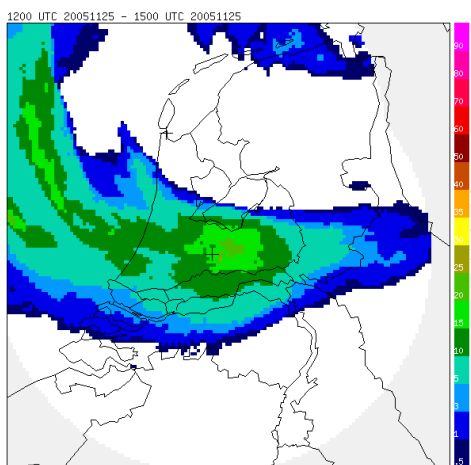
Range-weighted   Weighting factor
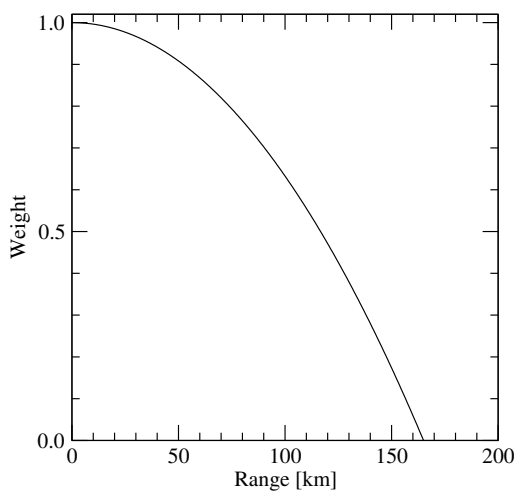
Figure 5.2: This figure shows examples of Maximum, Mean, and Range-weighted composites of bias adjusted accumulations from the radars in De Bilt and Den Helder (see Figure 5.1). The lower-right frame of the figure displays the weighting factor as a function of range as used for the range-weighted composite.

31

Range-weighted Use a range-weighted mean of the available pixel values in the composite product. In both the Maximum and Mean composites, discontinuities at the edge of the coverage of a radar sometimes occur. A range-weighted mean where the weight of the radar data gradually decreases with increasing range can be used to suppress these discontinuities in the composite.

In Figure 5.2 examples of Maximum (upper-left), Mean (upper-right), and Range-weighted (lower-left) composites of bias-adjusted precipitation accumulation products are presented. The accumulation products from the weather radars in De Bilt and Den Helder for 1500 UTC on 25 November 2005 (see Figure 5.1). have been used to build these composites. The lower-right frame displays the weighting factor as a function of range from the weather radar as used for the range-weighted composites. The weighting factor as a function of range $W(r)$ is calculated from:

$$ W(r) = \begin{cases} 1 - \left(\frac{r}{R_x}\right)^2 & \text{if } r \leq R_x \\ 0 & \text{if } r > R_x \end{cases} \qquad (5.1) $$

where R_x represents the maximum quantitative range (see Table 3.1). The data quality as a function of radar range is approximated by a quadratic function taking into account the increasing height and volume of the radar beam with increasing range. It is evident from the three images in Figure 5.2 that the Maximum composite contains, as expected, the highest precipitation depths. Furthermore, a discontinuity can be seen in the Eastern part of the maximum and mean composites, i.e., at the edge of the coverage of the Den Helder radar. In the range-weighted composite this discontinuity is absent and a smooth transition between coverage by two radars and coverage by only the De Bilt radar is made. Thus from a qualitative point of view the range-weighted composite is clearly preferred for accumulation products.

5.2 Processing flow of bias-adjusted accumulations

When we consider the 5-minute pseudoCAPPI products from the weather radars to be the beginning of the processing chain for the bias-adjusted accumulation composites, a processing chain consisting of four "links" remains. These different links, i.e., accumulation, post processing, bias adjustment, and compositing, have all been discussed in this report. Figure 5.3 gives a schematic overview of the processing chain for the bias-adjusted composites.
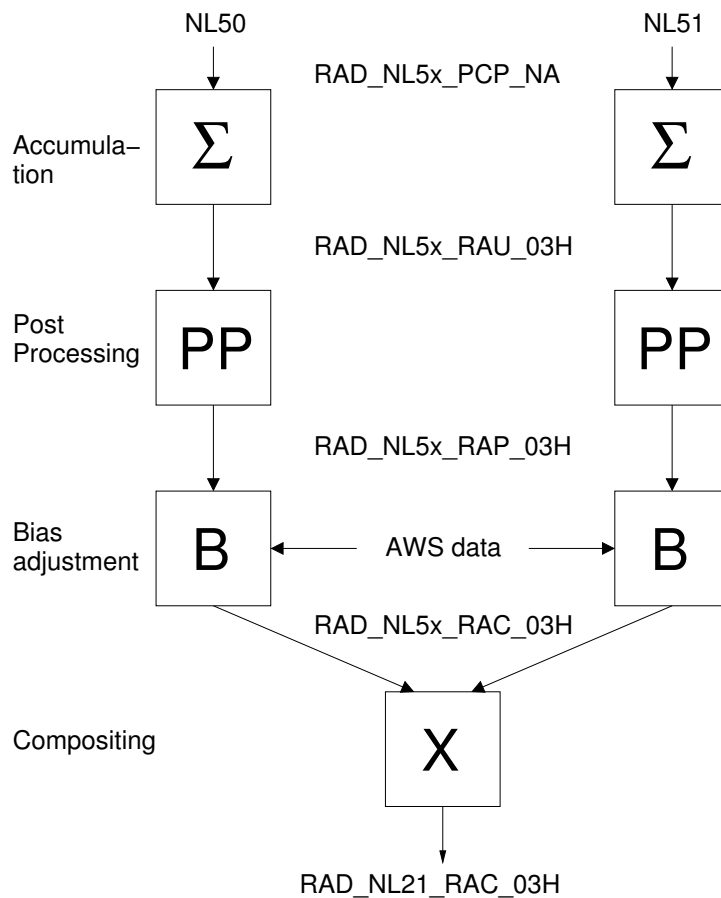
Figure 5.3: Schematic view of the processing chain for the bias-adjusted accumulation composites. The left chain represents De Bilt (NL50) and the right chain Den Helder (NL51).

The left chain refers to the processing of the radar in De Bilt (NL50) and the right chain to that of Den Helder (NL51). All weather radar products are available in the HDF5 format (http://hdf.ncsa.uiuc.edu/HDF5). The product names of the (intermediate) products in accordance with the KNMI HDF5 data model (Roozekrans and Holleman, 2003) are listed in the middle column of the scheme.

The processing chain for the bias-adjusted accumulation composites is mostly straightforward, and only the succession of the bias correction needs some explanation. In the proposed processing chain the bias-adjustment is performed individually for each weather radar. Alternatively, a common bias-adjustment could be performed after the compositing. The former has the

advantage that differences between weather radars due to e.g. (poor) calibration are cured. The latter has the advantage that possible biases introduced by the compositing method are corrected. However, by a proper choice of the compositing method hardly any bias is introduced by this process (see next chapter).

Chapter 6

Evaluation of bias-adjusted composites

A dataset containing 6 years (2000-2005) of weather radar accumulations and rain gauge observations has been used to evaluate the performance of the bias-adjustment algorithm and to verify the bias-adjusted radar composites of accumulated precipitation. First, the dataset is described and the performance of the bias-adjustment algorithm is evaluated by intercomparison of the two weather radars. Then the impact of the applied compositing method, i.e., Maximum, Mean, or Range-weighted, is assessed. Furthermore, the results of the verification of the bias-adjusted radar composites against 6 years of (in)dependent rain gauge observations are presented. Performances matrices are used to evaluate the bias-adjusted composites for different precipitation depth classes. Finally, the temporal and spatial variation of the quality of the bias-adjusted composites is investigated.

6.1 Validation of the bias-adjustment algorithm

The operational KNMI archive contains the 5-minute pseudoCAPPI products in HDF5 format with full resolution (256 reflectivity levels) from May 2003 up to now, and before this date the so-called "ERAS" products containing only 6 reflectivity levels are available in the archive. For the calculation of quantitative precipitation estimates, one absolutely needs the full resolution data and thus the ERAS products are not suited for this application. A non-operational archive containing 5-minute pseudoCAPPI products of both radars in so-called "PIF" format with full resolution was obtained and the PIF files have been converted to KNMI HDF5 format. This PIF archive starts
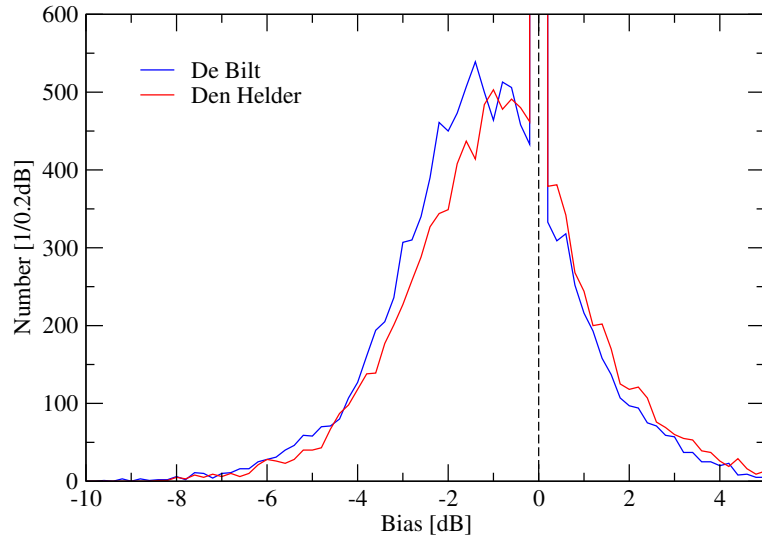
Figure 6.1: Histograms with the distribution of the obtained bias-adjustment factors for the radars in De Bilt (blue curve) and Den Helder (red curve) are shown. The 6-year dataset (2000-2005) of bias-adjusted 3-hour precipitation accumulations has been used for this figure. The histograms are constructed using a bin size of 0.2 dB. The off-scale peak at 0 dB reaches to 41320 and 42094 for De Bilt and Den Helder, respectively.

on 1 January 2000 and ends somewhere in October 2003, and unfortunately it contains some "gaps" here and there. Based on this (partly) operational archive of 5-minute pseudoCAPPI products in HDF5 format, "raw" 3-hour accumulations have been calculated every hour for both radars (De Bilt and Den Helder) between 1 January 2000 and 31 December 2005. In this way, 52294 and 52574 accumulation products have been obtained for De Bilt and Den Helder, respectively. Note that 52608 is the maximum number of hourly products over this period.

These "raw" precipitation accumulations have all been treated according to the processing chain depicted schematically in Figure 5.3. For this hourly precipitation depth observations from the automatic rain gauges over the 6 years have been used. These hourly observation have been accumulated to obtain the 3-hour precipitation depths. During the bias adjustment of the post-processed accumulations, the obtained bias-adjustment factors have been collected. Figure 6.1 shows two histograms with the distribution of these factors for the radars in De Bilt and Den Helder. The off-scale peak at 0 dB, i.e., no adjustment, reaches to 41320 and 42094 for De Bilt and Den Helder, respectively. Taking into account the number of available accumula-
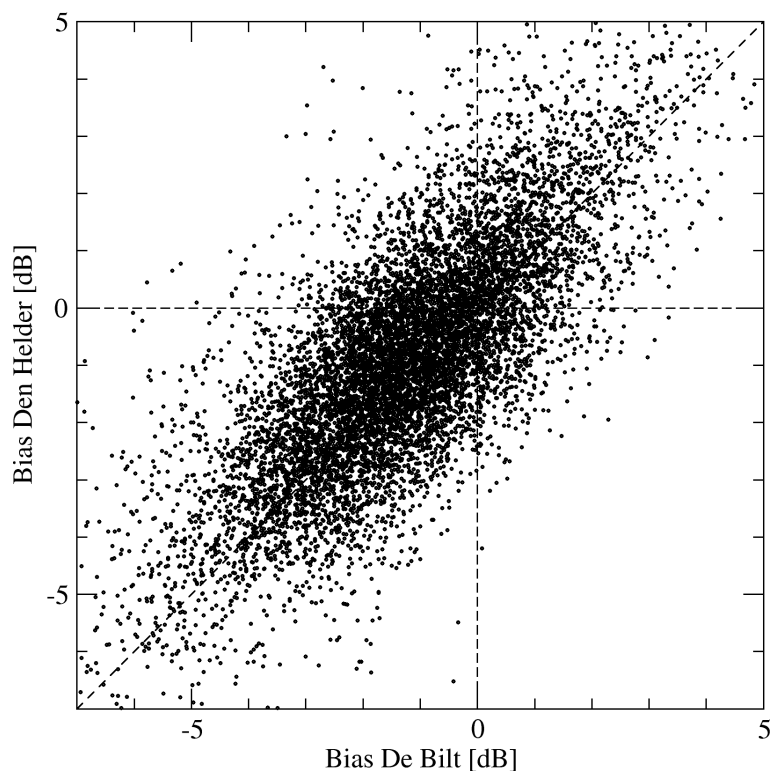
Figure 6.2: This scatter plot shows the correlation between the bias-adjustment factor for the De Bilt radar and that for the Den Helder radar. The 6-year dataset (2000-2005) of bias-adjusted 3-hour precipitation accumulations has been used for this figure. Only pairs where both bias factors are non-unity, i.e, not equal to 0 dB, have been plotted.

tion products, it is seen that a bias adjustment is performed on about 20% of the products. It is evident from Figure 6.1 that the long-term distribution (6 years) of bias-adjustment factors is rather similar for De Bilt and Den Helder. The distribution is rather broad with a full width at half maximum of about 4 dB and it is shifted towards negative dB-values. The latter indicates that the weather radars are underestimating the precipitation depths on average. This underestimation is due to the non-uniform Vertical Profile of Reflectivity (see Section 2.2). It should be noted that no real outliers, e.g. a bias-adjustment factor of -10 dB or so, are seen.

The distribution for De Bilt in Figure 6.1 is shifted to slightly more negative values suggesting that the underestimation by this radar is somewhat stronger. This is supported by the scatter plot between the bias-adjustment factors of De Bilt and of Den Helder as shown in Figure 6.2. Only pairs

Table 6.1: Verification of composited accumulations ($08-08$ UTC) between 2000 and 2005 against automatic rain gauges (dependent data). The mean daily precipitation depth, bias, and standard deviation are listed in mm. A total of 47547 gauge observations have been used for the verification. Results for "raw" accumulations composites using Mean algorithm, i.e., the operational product between June 2003 and April 2006, are given for reference.

Algorithm	Mean	Bias	Std.Dev.
Maximum	2.63	0.30	1.99
Mean	2.28	-0.04	1.79
Range-weighted	2.34	0.01	1.79
Raw	1.68	-0.65	2.57

where both bias-adjustment factors are not equal to 0 dB are plotted. The geographical coverages of both radars are overlapping to a large extent. If the observed biases are primarily due to meteorological phenomena, a good correlation between the biases of both radars should be found. A reasonable correlation between the bias-adjustment factors of both radars is evident from the figure. A correlation coefficient of $r = 0.76$ is found for the 6-year period under investigation. The majority of the scatter pairs shows up above the $y = x$ diagonal because the bias of De Bilt is on average more negative than the bias of Den Helder (difference about 0.4 dB). This difference may be due to a calibration difference but could also be caused by the larger fraction of land surface covered by the De Bilt radar.

6.2 Comparison of compositing algorithms

In Section 5.1 the performance of different compositing algorithms for accumulation products has been evaluated qualitatively. In this section results of a quantitative comparison of the compositing algorithms will be described. The 3-hour accumulation products are aggregated into 24-hour accumulations running from 08 to 08 UTC to enable a quantitative verification against the independent climatological rain gauge network (see Figure 4.1). Only 8 out of 24 accumulation products per day, i.e., the products ending at 11, 14, 17, 20, 23, 02, 05, and 08 UTC, are used to build the daily accumulations. For verification with the dependent data, the hourly observations from the automatic rain gauge network have been accumulated to obtain the daily $08-08$ UTC precipitation depths as well.

In Table 6.1 the results of a quantitative verification of the different compositing algorithms are listed and the results for the unadjusted accumulations, i.e., without post processing and bias adjustment, are added for reference. The radar composites have been verified against 6 year of automatic rain gauge data and a total of 47547 gauge observations have been used. The mean daily precipitation depth, bias, and standard deviation are listed. It should be noted that this verification against the rain gauge observations is a "dependent verification" because these data have been used for the bias adjustment of the individual radar accumulation products. The biases in Table 6.1 have been calculated according to Equation 4.2. It is evident from the table that the Maximum composite has a relatively large positive bias and that the biases of the Mean and Range-weighted composites are particularly small. The observed positive bias is in accordance with expectations and is inherent to the Maximum compositing algorithm (see Section 5.1). The standard deviation is also somewhat higher for the Maximum composites. The range-weighted algorithm performs the best in the quantitative comparison. The range-weighted compositing algorithm was also preferred from qualitative arguments (see Section 5.1) and therefore it is selected as the default compositing algorithm for accumulation products.

6.3 Verification of bias-adjusted composites

The bias-adjusted composites of accumulated precipitation have been verified against data from the automatic rain gauge network and the climatological rain gauge network. Because the former network has been used for the bias adjustment of the radar accumulations, this "dependent" verification provides a health-check of the bias-adjustment and compositing procedures. Verification against the latter network provides a truly independent verification of the bias-adjusted composites. In accordance with the conclusion from the previous section, the bias-adjusted composites have been generated using the range-weighted algorithm. To enable the quantitative verification against the independent climatological rain gauge network, the 3-hour accumulation products have been aggregated into 24-hour accumulations running from 08 to 08 UTC. Only days where both weather radars have contributed at least 280 (out of maximum 288) 5-minute pseudoCAPPI products to the accumulation product are included in the quantitative verification.

In Figure 6.3 scatter plots of the raw accumulations (left frame) and the adjusted accumulations (right frame) against the automatic gauge observations are shown. The scatter plot of the raw accumulation product against the automatic gauge observations reveals a major underestimation
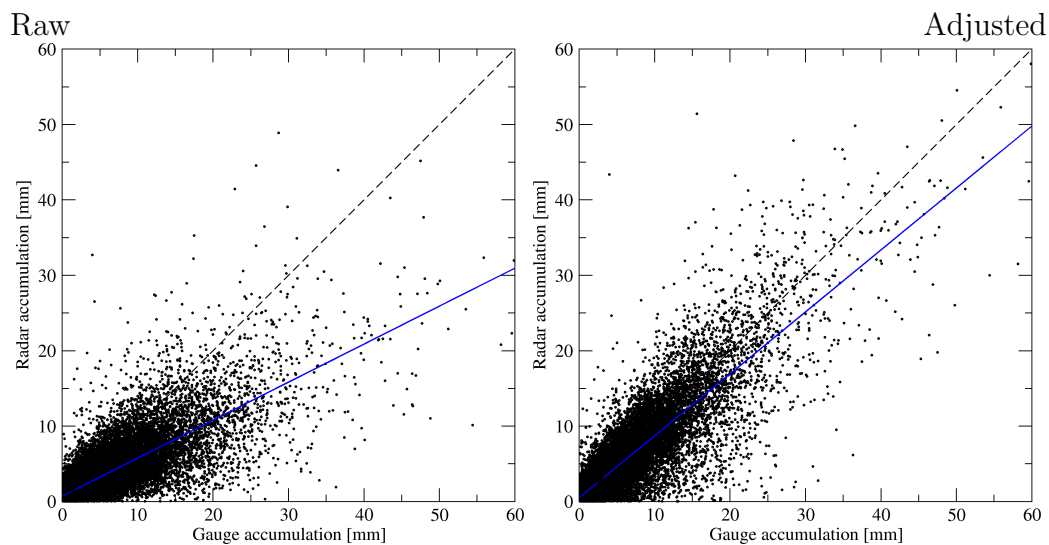
Raw   Adjusted

Figure 6.3: Scatter plot of the adjusted (right frame) and raw (left frame) radar accumulations against the collocated gauge observations. The observations from the automatic rain gauge network have been used. The 3-hour accumulation products have been aggregated into 24-hour accumulation $(08 - 08$ UTC). The blue lines represent least-squares fits to the scattered points.

of the $08 - 08$ UTC precipitation depths based on radar. About one-third (10313 out of 33453) of the scattered points lies above the dashed diagonal ($y = x$ identity line). The blue line in this figure represents a linear fit of the scattered points using the least-squares method. Although the correlation ($r = 0.79$) is pretty good, the fitted slope of this line is 0.50 which quantifies the major underestimation of the raw accumulations. The scatter plot of the bias-adjusted accumulations (right frame of Figure 6.3) looks quite different. The distribution of scatter points below and above the identity line is approximately fifty-fifty, 15715 points out of 33124 lie above this line. In addition, the points appear evenly scattered around the identity line. The least-squares fit gives a good correlation of $r = 0.87$ and a fitted slope of 0.82. Although this slope is approaching unity it is not as close as suggested by the figure. The known sensitivity of the least-squares methods (Press *et al.*, 1992) to outliers may be the rationale for this finding.

Table 6.2 lists the mean daily precipitation depth, the bias, and the standard deviation from the adjusted and raw accumulation products for each year in the verification dataset. The bias and standard deviation have been calculated using the automatic rain gauge observations. For the raw accu-

Table 6.2: Verification results for adjusted and raw accumulation composites against the dependent dataset, i.e., automatic gauge network. The complete dataset between 2000 and 2005 has been used. The mean daily precipitation depth, bias, and standard deviation are listed in mm. The number of gauge observations used for the verification is listed in the fifth column.

	Adjusted				Raw		
Year	Mean	Bias	Std.Dev.	Number	Mean	Bias	Std.Dev.
2000	2.32	0.06	1.71	7840	1.85	-0.41	1.99
2001	2.58	-0.01	1.70	8480	1.79	-0.80	2.46
2002	2.76	0.01	2.17	5728	2.00	-0.76	3.14
2003	1.82	0.07	1.54	7552	1.47	-0.27	2.15
2004	2.46	0.00	1.81	9063	1.62	-0.83	2.77
2005	2.17	-0.06	1.84	8884	1.44	-0.78	2.79
All	2.34	0.01	1.79	47547	1.68	-0.65	2.57

Table 6.3: Verification results for adjusted and raw accumulation composites against the **in**dependent dataset, i.e., climatological gauge network. The complete dataset between 2000 and 2005 has been used. The mean daily precipitation depth, bias, and standard deviation are listed in mm. The number of gauge observations used for the verification is listed in the fifth column.

	Adjusted				Raw		
Year	Mean	Bias	Std.Dev.	Number	Mean	Bias	Std.Dev.
2000	2.37	-0.03	1.95	80510	1.88	-0.53	2.14
2001	2.63	-0.12	1.96	87184	1.81	-0.93	2.58
2002	2.81	-0.10	2.39	58891	2.02	-0.89	3.15
2003	1.86	-0.04	1.66	77643	1.48	-0.43	2.16
2004	2.65	-0.23	2.21	64394	1.70	-1.18	3.24
2005	2.35	-0.24	2.03	64437	1.54	-1.05	3.03
All	2.43	-0.12	2.02	433059	1.73	-0.82	2.72

mulations, a serious mean-field bias of roughly 40% of the mean precipitation depth is found for all years. The standard deviation is substantially larger than the mean precipitation depth. It is evident that no significant mean-field bias is left in the adjusted accumulation composites. The standard deviation has been reduced as well by the bias adjustment procedure and it is now substantially smaller than the mean precipitation depth. The number of gauge observations used for verification varies from year to year because only days where both radars have contributed at least 280 pseudoCAPPI products are included. The results of the independent verification using the climatological gauge network are listed in Table 6.3. Generally the results are similar to those in Table 6.2 but a few differences can be seen. The bias of the adjusted accumulations is not exactly zero, i.e. about 5% of the mean precipitation depth, for the independent verification. This small negative bias can be explained by the observed differences between the automatic and climatological rain gauges (Bruin, 2002). Naturally the standard deviations of the accumulation composites against the independent rain gauge network are somewhat higher, but for the adjusted accumulations they are still substantially lower than the mean daily totals.

6.4 Performance matrices for bias-adjusted composites

The capability of the radar accumulation products in observing certain classes of precipitation depths has been evaluated using so-called performance matrices or contingency tables. Table 6.4 shows the performance matrix obtained for the raw accumulation products against the climatological gauge network. Six precipitation depth classes, $0 - 0.5$, $0.5 - 10$, $10 - 20$, $20 - 30$, $30 - 40$, and > 40 mm, have been used to construct the performance matrix. Each cell in the matrix denotes the number of events obtained during the verification period (2000-2005). In case of full agreement between radar and gauge networks, i.e., in an ideal world, all off-diagonal elements would be zero. The ratio between the on-diagonal events and the total number of events, the so-called fraction correct, is 0.847. In addition, it is evident from the matrix that the number of events above the diagonal (47342) is almost three times larger than that below the diagonal (18187). This is again caused by the major underestimation of the precipitation depths by the raw radar accumulations. The performance matrix of the bias-adjusted accumulation composites is given in Table 6.5. It is immediately clear from the matrix that the events are distributed much more evenly below and above the di-

Table 6.4: Performance matrix for the raw accumulation composites against the climatological rain gauge observations. Six classes of daily precipitation depth, denoted in mm, are used. A total of 433059 gauge observations between 2000 and 2005 have been used for this table.

		Gauges					
		$0 - 0.5$	$0.5 - 10$	$10 - 20$	$20 - 30$	$30 - 40$	> 40
	$0 - 0.5$	216321	24428	14	1	0	0
	$0.5 - 10$	15950	144374	17038	1515	184	39
	$10 - 20$	8	1793	6328	2783	608	165
Radar	$20 - 30$	3	47	303	406	283	206
	$30 - 40$	0	4	23	32	68	78
	> 40	0	0	3	6	15	33

Table 6.5: Performance matrix for the adjusted accumulation composites against the climatological rain gauge observations. Six classes of daily precipitation depth, denoted in mm, are used. A total of 433059 gauge observations between 2000 and 2005 have been used for this table.

		Gauges					
		$0 - 0.5$	$0.5 - 10$	$10 - 20$	$20 - 30$	$30 - 40$	> 40
	$0 - 0.5$	217012	19199	7	1	0	0
	$0.5 - 10$	15253	145209	7901	300	28	3
	$10 - 20$	15	6118	13918	2031	189	37
Radar	$20 - 30$	1	101	1739	1895	480	113
	$30 - 40$	1	12	122	466	342	154
	> 40	0	7	22	50	119	214
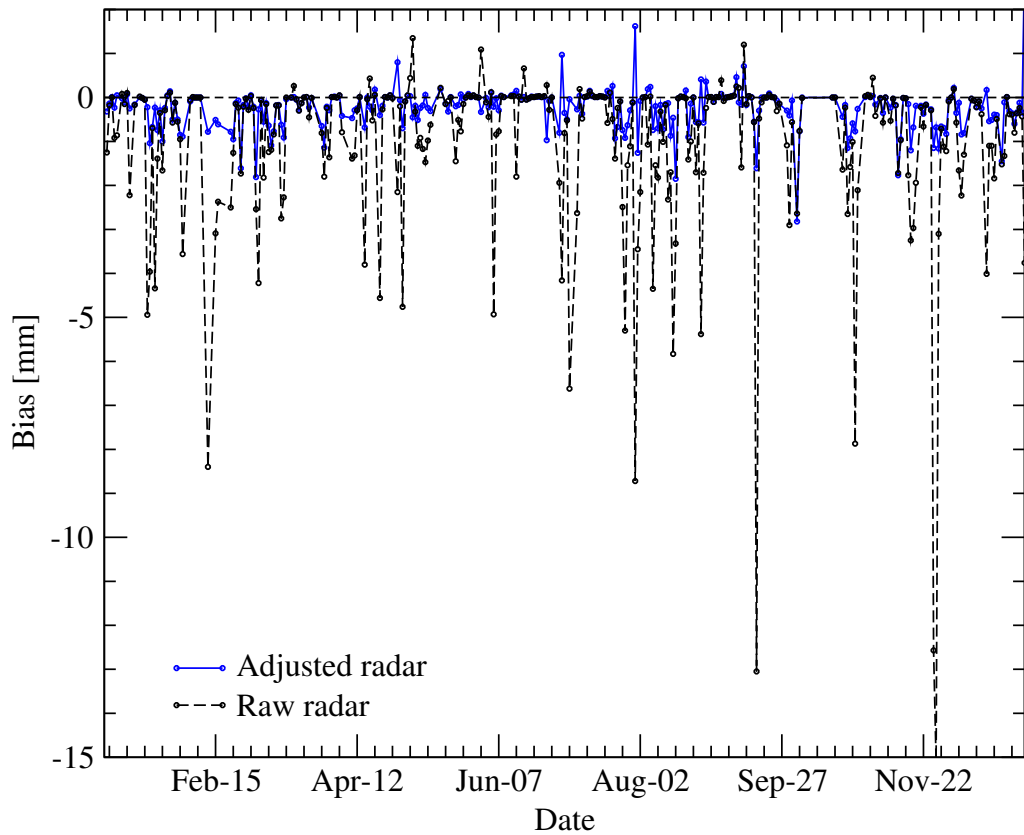
Figure 6.4: Bias of the adjusted (blue) and raw (black-dashed) radar accumulations against the independent, climatological gauge network as a function of day in 2005.

agonal. The number of events above the diagonal (30443) is still 27% larger than that below the diagonal (24026) which is most likely due to the small negative bias of the adjusted composites with respect to the climatological network (see Table 6.3). For the adjusted composites, the fraction correct is 0.874 which is only marginally better than before. This is due to the large number of "dry" events in the $0 - 0.5$ mm range.

6.5   Temporal evolution of mean-field bias

To relate the quality of radar accumulation products to meteorological circumstances, the bias and standard deviation have been calculated per day for 2005. Figure 6.4 shows the daily bias of the adjusted (blue) and raw

Biases   Standard deviations
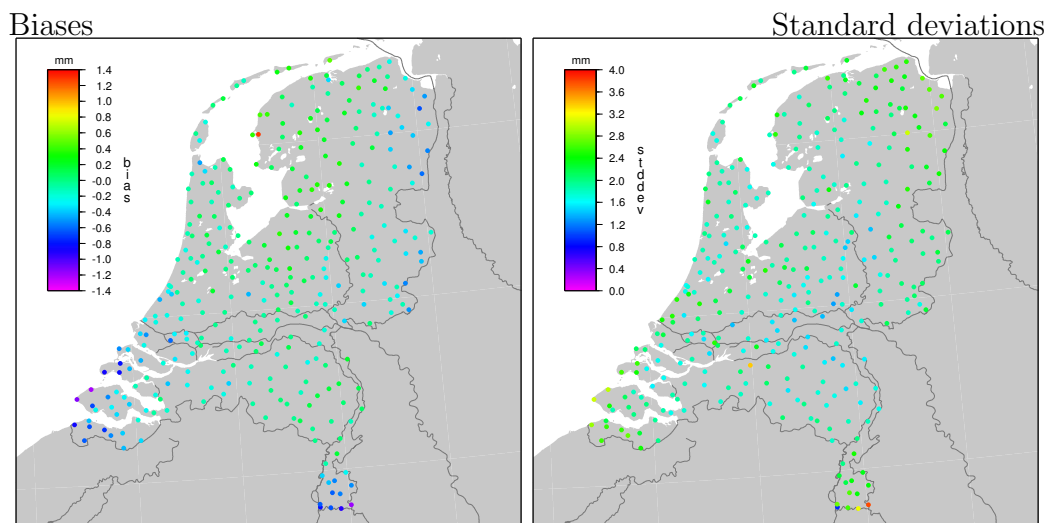
Figure 6.5: This figure shows two maps of the biases (left frame) and standard deviations (right frame) of the bias-adjusted accumulation composites against the climatological rain gauge network. Data from the whole verification period (2000-2005) have been used. Biases and standard deviations are given in mm.

(black dashed) radar accumulations with respect to the climatological gauge network. The largest underestimation of the raw radar accumulation is seen on 25-26 November 2005 which is the winter storm case used throughout this report. It is evident that the underestimation is occasionally very substantial, i.e., 10 mm or more. In contrast, the daily bias of the adjusted accumulations is typically (much) smaller than 1 mm and hardly ever it is larger than that of the raw accumulations. So especially in cases of extreme underestimation of the raw radar products the bias-adjustment procedure has a large positive impact.

6.6   Spatial dependence of the performance

The (non-uniform) Vertical Profile of Reflectivity (VPR), depending mainly on the meteorological circumstances, and the increasing height of radar observations with increasing range make that quality of radar-based quantitative precipitation estimates depends strongly on range. To assess the spatial variability of the quality of the bias-adjusted accumulation composites, the bias and standard deviation of these composites have been calculated for each individual climatological rain gauge.

45

Figure 6.5 shows the biases (left frame) and standard deviations (right frame) of the bias-adjusted accumulation composites against the climatological rain gauge network. The colored dots in the maps indicate either the bias or the standard deviation for the underlying rain gauge. When we focus on the left map with the biases, slightly positive values (green dots) are seen in the central parts of The Netherlands and substantial underestimation (blue-purple) is seen in southwest, southeast, and northeast corners of The Netherlands. The station in Makkum (northwest) gives a clear outlier (red dot) which is due to semi-permanent residual clutter from anomalous propagation of the Den Helder radar over the "IJsselmeer". The values of the station biases and standard deviations should be related to the mean daily precipitation depth of 2.43 mm (see Table 6.3). The observed pattern is consistent with a slight overestimation at short range and a (substantial) underestimation at long range from the weather radars. The mean-field bias adjustment method cannot correct for this range dependency of the bias. A VPR correction procedure based on physical algorithms is needed to (partly) correct for these range dependencies.

The right map with the standard deviations reveals a more homogeneous distribution and only on the southern edge of The Netherlands a few high values are seen. The station in Capelle (just south of the rivers) is a clear outlier (orange dot). The lowest standard deviations (blue dots) are seen in the southern part and western part of The Netherlands and somewhat higher values are seen in northeast, southwest, and central parts of The Netherlands. The standard deviation of a radar-gauge comparison is largely due to representativeness errors, i.e., differences in the sampled volumes (Kitchen and Blackall, 1992). The siting of the rain gauge, which determines the importance of the local environment, and the range from the radar, which determines the size of the sampled volume, are the main factors. Post processing and mean-field bias-adjustment can reduce the standard deviation to a certain extent, but physical algorithms, e.g. local downscaling (similar to wind data), are required to reduce the representativeness error.

Chapter 7

Conclusions and Recommendations

The non-uniform Vertical Profile Reflectivity, the conversion of radar reflectivity Z to rainfall rate R, and the attenuation due to strong precipitation are the major sources of error in quantitative precipitation estimation. Adjustment methods for non-uniform VPR are still topic of research and operational application is currently in its infancy. The impact of the last two sources of error can be reduced considerably by operation of a so-called Dual-Polarization weather radar (Bringhi and Chandrasekar, 2001), but it will probably take another 10 years before KNMI will operate this type of radar. In this technical report it has been demonstrated that the quality of the 3-hour accumulation product can be significantly enhanced by a gauge adjustment procedure.

The quality of the bias-adjusted 3-hour accumulation products has been evaluated using both (in)dependent gauge observations. A 6-year dataset of bias-adjusted accumulation products between 2000 and 2005 was used for the verification. It is concluded that the proposed scheme effectively removes the mean-field bias from the raw accumulation products and that it substantially reduces the standard deviation. The mean-field bias varies strongly from day-to-day depending on the meteorological conditions. From a spatial analysis it is concluded that the quality of the product degrades with increasing range. The quantitative precipitation estimates on the borders of The Netherlands, i.e., Limburg, Zeeland, and east Groningen, are already affected by this degradation.

Based on the findings in this technical report the following recommendations are made:

- Add the bias-adjustment procedure using automatic rain gauges to the

0800 UTC   1400 UTC
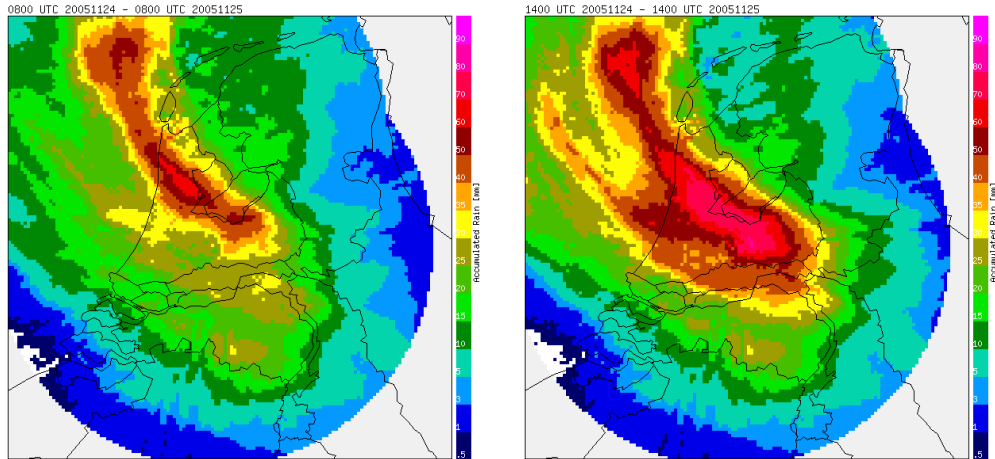
Figure 7.1: Two images showing bias-adjusted accumulation composites for 25 November 2005. The left image shows the 24-hour accumulation ending at 0800 UTC, i.e., synchronous with the climatological rain gauge network, and the right images shows the 24-hour accumulation with the largest precipitation depths (ending at 1400 UTC).

operational 3-hour accumulation product (Done on 1 April 2006).

- Use the bias-adjusted accumulation product instead of the raw accumulations for monitoring of severe weather, feeding of automated warning systems (Done for "Gevaarlijk Weer voor Waterbeheer"), and deliveries to external customers.

- Increase the target height of the pseudoCAPPIs for accumulation products from 800 to 1500 meter in order to reduce the range dependency of the bias.

- Perform Research & Development on physical VPR adjustment algorithms suited for operational implementation.

- Look out for improved algorithms for $Z - R$ conversion and attenuation correction in scientific literature.

- Monitor experiences of other (European) National Meteorological Services with operational Dual-Polarization weather radars, e.g. within EUMETNET OPERA.

Finally, an example of the benefit of hourly updated precipitation accumulations over fixed $08 - 08$ UTC accumulations is presented in Figure 7.1. The left image shows the 24-hour accumulation ending at 0800 UTC and the right images shows the 24-hour accumulation ending at 1400 UTC on 25 November 2005. It is evident that much larger areas with higher precipitation depths are observed in the right image. Thus the real-time bias-adjusted accumulation product can be a great help in the monitoring and evaluation of strong precipitation events.

Acknowledgments

References

Andrieu, H. and J. D. Creutin, 1995: Identification of vertical profiles of radar reflectivity for hydrological applications using an inverse method. Part I: Formulation. *J. Appl. Meteor.*, **34**, 225–239.

Atlas, D. and C. W. Ulbrich, 1977: Path- and area-integrated rainfall measurement by microwave attenuation in the 1-3 cm band. *J. Appl. Meteor.*, **16**, 1322–1331.

Benschop, H., ed., 2000: *Handbook for the Meteorological Observation*, KNMI, chapter 6. 91–112, available via http://www.knmi.nl/samenw/hawa.

Berne, A. and R. Uijlenhoet, 2006: Quantitative analysis of X-band weather radar attenuation correction accuracy. *Nat. Hazards Earth Syst. Sci.*, **6**, 419–425.

Bringhi, V. N. and V. Chandrasekar, 2001: *Polarimetric Doppler weather radar*. Cambridge Univ. Press, U.K., 636 pp.

Browning, K. A., 1987: *Weather Radar and Flood Forecasting*, John Wiley & Sons, chapter Towards a more effective use of radar and satellite imagery in weather forecasting. 239–269.

Bruin, A. T. H., 2002: Veranderingen in neerslagkarakteristieken in Nederland gedurende de periode 1901-2001. Technical report TR-246, Royal Netherlands Meteorological Institute (KNMI), 42 pp.

Chumchean, S., A. Sharma, and A. Seed, 2006: An integrated approach to error correction for real-time radar-rainfall estimation. *J. Atmos. Ocean. Technol.*, **23**, 67–79.

Collier, C. G., 1989: *Applications of Weather Radar Systems: a Guide to Uses of Radar Data in Meteorology and Hydrology*. John Wiley & Sons, West Sussex, England.

Delrieu, G., L. Hucke, and J. D. Creutin, 1999: Attenuation in rain for X-band and C-band weather radar systems: Sensitivity with respect to the drop size distribution. *J. Appl. Meteor.*, **38**, 57–68.

Doviak, R. J. and D. S. Zrnić, 1993: *Doppler Radar and Weather Observations*, second edition. Academic Press, 562 pp.

Evenden, G. I., 1990: Cartographic projection procedures for the UNIX environment — a users's manual. Technical report, United States Department of the Interior Geological Survey (USGS), www.remotesensing.org/proj/.

Fulton, R. A., J. P. Breidenbach, D.-J. Sea, D. A. Miller, and T. O'Bannon, 1998: The WSR-88D rainfall algorithm. *Wea. and. Forecasting*, **13**, 377–395.

Gematronik, 2003: Rainbow 3.4 operator's manual. Gematronik GmbH., Raiffeneisenstr. 10, 41470 Neuss, Germany, 215 pp., release 4.7.

Germann, U., 1999: Radome attenuation — a serious limiting factor for quantitative radar measurements? *Meteor. Zeitschrift*, **8**, 85–90.

Gorgucci, E., G. Scarchilli, V. Chandrasekar, P. F. Meischner, and M. Hagen, 1998: Intercomparison of techniques to correct for attenuation of C-band weather radar signals. *J. Appl. Meteor.*, **37**, 845–853.

Harrison, D. L., S. J. Driscoll, and M. Kitchen, 2000: Improving precipitation estimates from weather radar using quality control and correction techniques. *Meteor. Appl.*, **6**, 135–144.

Hitschfeld, W. and J. Bordan, 1954: Errors inherent in the radar measurement of rainfall at attenuating wavelenghts. *J. Meteorol.*, **11**, 58–67.

Holleman, I., 2003: Neerslaganalyse uit radar- en stationswaarnemingen. Internal report IR-2003-06, Royal Netherlands Meteorological Institute (KNMI), 25 pp.

— 2004: VPR adjustment using a dual CAPPI technique. *ERAD Publication Series*, **2**, 25–30.

Holleman, I. and H. Beekhuis, 2004: Weather radar monitoring using the sun. Technical report TR-272, Royal Netherlands Meteorological Institute (KNMI), 40 pp.

— 2005: Review of the KNMI clutter removal scheme. Technical report TR-284, Royal Netherlands Meteorological Institute (KNMI), 52 pp.

Huuskonen, A. and I. Holleman, 2006: Determining weather radar antenna pointing using signals detected from the sun at low antenna elevations. *J. Atmos. Ocean. Technol.*, in press.

Joe, P., 1996: *Precipitation at the Ground: Radar Techniques*, Springer NATO ASI Series, chapter 12. 277–321.

Joss, J. and A. Waldvogel, 1990: *Radar in Meteorology*, AMS Boston, chapter Precipitation Measurement and Hydrology. 577–606.

Kitchen, M. and R. M. Blackall, 1992: Representativeness errors in comparisons between radar and gauge measurements of rainfall. *J. Hydrol.*, **134**, 13–33.

Kitchen, M., R. Brown, and R. G. Davies, 1994: Real-time corrections of weather radar data for the effects of bright band, range and orographic growth in widespread precipitation. *Q. J. R. Meteorol. Soc.*, **120**, 1231–1254.

Koistinen, J., 1991: Operational correction of radar rainfall errors due to the vertical reflectivity profile. *25th conference on Radar Meteorology*, Amer. Meteor. Soc., 91–94.

Koistinen, J., H. Pohjola, and H. Hohti, 2003: Vertical reflectivity profile classification and correction in radar composites in Finland. *31st conference on Radar Meteorology*, Amer. Meteor. Soc., 534–537.

Manz, A., T. Monk, and J. Sangiolo, 1998: Radome effects on weather radar systems. *COST 75 international conference, Locarno*, EC, 467–478.

Marshall, J. S. and W. M. Palmer, 1948: The distribution of raindrops with size. *J. Atmos. Sci.*, **5**, 165–166.

Michelson, D., T. Einfalt, I. Holleman, U. Gjertsen, K. Friedrich, G. Haase, M. Lindskog, and A. Jurczyk, 2005: Weather radar data quality in Europe: Quality control and characterization. Technical Report EUR 21955, EU (Brussels), 92 pp.

Michelson, D. B., T. Andersson, J. Koistinen, C. G. Collier, J. Riedl, J. Szrurc, U. Gjertsen, A. Nielsen, and S. Overgaard, 2000: BALTEX Radar Data Centre Products and their methodologies. Report RMK No. 90, Swedish Meteorological and Hydrological Institute (SMHI).

Press, W. H., S. A. Teukolsky, W. T. Vetterling, and B. P. Flannery, 1992: *Numerical Recipes in C: the Art of Scientific Computing*, second edition. Cambridge University Press, 994 pp.

Roozekrans, H. and I. Holleman, 2003: KNMI HDF5 data format specification, v3.5. Internal report IR-2003-05, Royal Netherlands Meteorological Institute (KNMI), 30 pp.

Sigmet, 1998: RVP6 doppler signal processor user's manual. Sigmet Inc., 2 Park Drive, Westford, MA 01886 USA, 208 pp., ROM Rev. 39.

Uijlenhoet, R., 1999: *Parametrization of Rainfall Microstructure for Radar Meteorology and Hydrology*. Ph.D. thesis, Wageningen University and Research centre (WUR), 279 pp., ISBN 90-5808-156-7.

Uijlenhoet, R. and J. N. M. Stricker, 1999: A consistent rainfall parameterization based on the exponential raindrop size distribution. *J. Hydrol.*, **218**, 101–127.

Vignal, B., H. Andrieu, and J. D. Creutin, 1999: Identification of vertical profiles of reflectivity from volume scan radar data. *J. Appl. Meteor.*, **38**, 1214–1228.

Vignal, B., G. Galli, J. Joss, and U. Germann, 2000: Three methods to determine profiles of reflectivity from volumetric radar data to correct precipitation estimates. *J. Appl. Meteor.*, **39**, 1715–1726.

Vignal, B. and W. Krajewski, 2001: Large-sample evaluation of two methods to correct range-dependent error for WSR-88D rainfall estimates. *J. Hydrometeor.*, **2**, 490–504.

Wessels, H. R. A., 1972: Metingen van regendruppels te De Bilt. Scientific report WR 72-6, Royal Netherlands Meteorological Institute (KNMI), 47 pp.

Wessels, H. R. A. and J. H. Beekhuis, 1994: Stepwise procedure for suppression of anomalous ground clutter. *COST-75 Seminar on Advanced Radar Systems*, EUR 16013 EN, 270–277.

Appendix A

Geographical projection of KNMI radar images

In this appendix the details of the geographical projection of the KNMI radar images, both single site data and the national composite, are listed. The radar images are projected according to a stereographic projection with the northpole in the projection origin. A stereographic projection also uses a so-called alignment meridian (Greenwich) which is equal to the longitude of the projection origin and a latitude of true scale (60N). The stereographic projection is a conformal projection which implies that the angles are conserved during the projection. The meridians are projected into straight lines starting from the north pole and latitude circles are projected as circles centered at the north pole. It is important to stress that the KNMI radar images are projected using an ellipsoide earth model (Hayford). This makes the projection equations substantially more complex, but it enables a more accurate overlay of the radar echoes with the topographical data. The parameters of the geographical projection of the KNMI radar images are listed in the table below:

Parameter	Value
Projection	Stereographic
Projection origin (lon,lat)	0E, 90N
True scale (lat)	60N
Earth radius (equator,polar)	6378.388 km, 6356.912 km
Pixel size at true scale (x,y)	2.500 km, −2.500 km
Offset of image corner (i,j)	0.0, 1490.9
Number of rows	256
Number of columns	256

The geographical projection of the radar data from the azimuthal equi-distance projection ("radar projection") to the polar stereographic projection can be done using the "proj.4" library (Evenden, 1990). This library has been developed at the USGS and is used world-wide in numerous applications. The geographical projection of the KNMI radar images is described by the following "proj.4 string":

```
"+proj=stere +x_0=0 +y_0=0 +lat_0=90 +lon_0=0 +lat_ts=60 +a=6378.388 +b=6356.906"
```

After the geographical (re)projection the resulting image only has to be scaled and shifted linearly using the given pixel sizes and offsets of the image corner. The pixel size in y-direction is negative because the images lines are plotted from north-to-south and the y-axis is pointing in the opposite direction. The projection parameters define the geographical corners of the KNMI radar images. The corners of the KNMI radar image are:

Corner	Lon [deg]	Lat [deg])
north-west	0.000E	55.296N
north-east	9.743E	54.818N
south-east	8.337E	49.373N
south-west	0.000E	49.769N